https://doi.org/10.1016/j.jsv.2022.117410
This is the Pre-Published Version.

Topology optimization of a second-order phononic topological insulator with dual-band corner states

Yafeng Chen[1,2], Jie Zhu[1,3*], Zhongqing Su[1†]

[1]*Department of Mechanical Engineering, Hong Kong Polytechnic University, Hong Kong, China*

[2]*State Key Laboratory of Advanced Design and Manufacturing for Vehicle Body, Hunan University, Changsha, Hunan 410082, China*

[3]*Institute of Acoustics, School of Physics Science and Engineering, Tongji University, Shanghai 200092, China*

Abstract

Second-order phononic topological insulators (SPTIs) with topologically protected corner states offer unique routes for the realization of steering elastic waves in lower-dimension regime with robustness. However, prevailing SPTIs only host corner states within a single bandgap, restricting applications of SPTIs in multiband domain. Here, we design four new types of SPTIs with the customized dual-bandgap which supports dual-band corner states. The dual-bandgap is created by simultaneously maximizing the minimum imaginary parts of wave vectors at two desired frequencies via topology optimization. Topological trivial and nontrivial unit cells (UCs), sharing the dual-bandgap, are configured by selecting UCs from the same optimized phononic crystals (PCs) in different ways. The dual-band topological corner states are observed at the corner between the trivial and nontrivial regions. The developed four SPTIs with customized dual-band operating frequencies pave the way for multiband communications and manipulation of elastic waves with enhanced robustness.

Keywords: Phononic crystals; High-order topological insulators; Topology optimization

* jiezhu@tongji.edu.cn
† zhongqing.su@polyu.edu.hk

© 2022. This manuscript version is made available under the CC-BY-NC-ND 4.0 license https://creativecommons.org/licenses/by-nc-nd/4.0/

1. Introduction

As artificially designed structural materials, phononic crystals (PCs) can exhibit extraordinary properties that natural materials cannot offer, providing great flexibility for steering elastic waves [1]. Recently, creating phononic topological insulators (PTIs), that is, realizing topological phases in the platform of PCs, becomes an exciting frontier of research [2]. By virtue of topologically protected modes that are robust against defects, PTIs offer opportunities for the realization of manipulating elastic waves with high-efficiency and robustness. To date, mimicking topological insulators in condensed matter physics, several kinds of PTIs have been achieved according to different physical schemes, e.g., quantum Hall effect (QHE) [3], quantum spin Hall effect (QSHE) [4] and quantum valley Hall effect (QVHE) [5]. Obeying to the bulk-boundary correspondence, these ATIs support gapless edge states that are topologically protected.

More recently, the high-order TIs (HOTIs) defying the conventional bulk-boundary correspondence have been realized [6, 7]. In a two dimensional system, the HOTI is called as second-order TI (SOTI), which supports 1D gapped edge states and 0D corner states. Then, the theory of HOTIs has been transplanted into the field of PCs. For creating the HOTIs, the crystalline symmetry performs a critical role. So far, several versions of second-order phononic TIs (SPTIs) have been created in various lattices with different symmetries, such as square lattice with C_2 symmetry [8], hexagon lattice with C_{6v} symmetry [9, 10] and hexagon lattice with C_3 symmetry [11, 12]. The realization of SPTIs offers new ways for manipulating elastic waves in lower dimensions with robustness. However, prevailing SPTIs only host corner states within one bandgap, limiting their potential applications in multiband communications, filters, waveguides, information processions and so forth. Moreover, in some applications, e.g. nonlinear frequency conversion, it is also desirable to design multiband topological modes [13,

14].

To overcome this challenge, in this paper, we design several SPTIs hosting dual-band topological corner states by topology optimization. As an inverse design technique aiming to find optimal material distributions to realize the best structural performance under the given constraints, topology optimization has been widely exploited in designing traditional civil and engineering structures [15], metastructures and metamaterials [16-24]. Recently, topology optimization has been exploited to design photonic, sonic and phononic TIs, such as photonic, sonic and phononic TIs based on QSHE [25-30], phononic TIs based on QVHE [31, 32] and second-order photonic and phononic TIs [33-35]. However, topology optimization of SPTIs hosting dual-band topological corner states has never been investigated. Previous studies show that the trivial and nontrivial unit cells for constructing the second-order photonic/phononic TI could be selected from the same photonic/phononic crystal hosting odd-order bandgap in different ways [14, 36-42]. Thus odd-order bandgap is the prerequisite for creating the SPTI. Herein, we firstly design PCs with the dual odd-order bandgaps by simultaneously maximizing minimum imaginary parts of wave vectors at two desired frequencies via topology optimization. Then, by choosing unit cells (UCs) from the optimized PCs in different ways, topological trivial and nontrivial UCs sharing the optimized dual-bandgap are created. Arranging the trivial and nontrivial UCs to construct the SPTI, dual-band topological edge and corner states are realized within the dual-bandgap. Totally, four SPTIs supporting dual-band topological corner states are designed. The remaining paper is given as follows: the complex band theory and topology optimization method are detailed in Section 2; the discussions on the optimized SPTIs are given in Section 3, followed by the conclusion in Section 4.

2. Theory and method

2.1 Complex band theory

For elastic wave propagating in two-dimensional PCs, the controlling equations can be classified into out-of-plane and in-plane modes [1, 43]. Here, we focus on the out-of-plane mode and its governing equation without external force is

$$\rho(\mathbf{r})\frac{\partial^2 u_z}{\partial t^2}=\frac{\partial}{\partial x}\left[\mu(\mathbf{r})\frac{\partial u_z}{\partial x}\right]+\frac{\partial}{\partial y}\left[\mu(\mathbf{r})\frac{\partial u_z}{\partial y}\right] \tag{1}$$

where $\mathbf{r}=(x,y)$ is the position vector. ρ is the density; μ is the shear modulus. Due to the periodicity of PCs, $\rho(\mathbf{r})=\rho(\mathbf{r}+\mathbf{R})$ and $\mu(\mathbf{r})=\mu(\mathbf{r}+\mathbf{R})$, in which $\mathbf{R}$ denotes the lattice translation vector. Following the Bloch' theorem [44],

$$u(\mathbf{r},\mathbf{k})=u_{\mathbf{k}}(\mathbf{r})e^{i(\omega t+\mathbf{k}\cdot\mathbf{r})} \tag{2}$$

where $\mathbf{k}=(k_x,k_y)$ denotes the wave vector. ω represents the angular frequency. $u_{\mathbf{k}}(\mathbf{r})=u_{\mathbf{k}}(\mathbf{r}+\mathbf{R})$ denotes the periodic displacement function, which has the same periodicity as the PC. Taking Eq. (2) into Eq. (1) gets an eigenvalue equation containing two unknown variables, i.e., $\mathbf{k}$ and ω, which could be solved by the $\omega(\mathbf{k})$ method or $\mathbf{k}(\omega)$ method [1]. The $\omega(\mathbf{k})$ method solves ω by sweeping $\mathbf{k}$ and gets the classical band structure, whereas the $\mathbf{k}(\omega)$ method solves $\mathbf{k}$ by sweeping ω and obtains the complex band structure [45-47]. As the optimization of our work is based on the complex band theory, we will describe the $\mathbf{k}(\omega)$ method herein. In the $\mathbf{k}(\omega)$ method, k_x and k_y are set as $k_x=k\cos\theta$ and $k_y=k\sin\theta$, as illustrate in Fig. 1(b), where θ denotes the wave vector direction and is a given value. Therefore, the $\mathbf{k}(\omega)$ method obtains the complex band structure at the given wave vector direction, θ. Adopting the finite element method, the eigenvalue equation could be formulated as

$$\left(k^2\mathbf{K}_{\mathrm{I}}+k\mathbf{K}_{\mathrm{II}}+\mathbf{K}_{\mathrm{III}}\right)\mathbf{u}=\mathbf{0} \tag{3}$$

in which **u** denotes the eigenvector of the displacement field. $\mathbf{K}_{\mathrm{I}}$, $\mathbf{K}_{\mathrm{II}}$ and $\mathbf{K}_{\mathrm{III}}$ can be expressed by

$$\mathbf{K}_{\mathrm{I}}=\left(\cos^2\theta+\sin^2\theta\right)\mathbf{K}_1 \tag{4a}$$

$$\mathbf{K}_{\mathrm{II}}=i\left(\cos\theta\mathbf{K}_2+\sin\theta\mathbf{K}_3\right) \tag{4b}$$

$$\mathbf{K}_{\mathrm{III}}=\mathbf{K}_4-\omega^2\mathbf{M} \tag{4c}$$

where

$$\mathbf{K}_1=\mu\int_A\left(\mathbf{N}^T\mathbf{N}\right)dA$$

$$\mathbf{K}_2=\mu\int_A\left(\frac{\partial\mathbf{N}^T}{\partial x}\mathbf{N}-\mathbf{N}^T\frac{\partial\mathbf{N}}{\partial x}\right)dA$$

$$\mathbf{K}_3=\mu\int_A\left(\frac{\partial\mathbf{N}^T}{\partial y}\mathbf{N}-\mathbf{N}^T\frac{\partial\mathbf{N}}{\partial y}\right)dA$$

$$\mathbf{K}_4=\mu\int_A\left(\frac{\partial\mathbf{N}^T}{\partial x}\frac{\partial\mathbf{N}}{\partial x}+\frac{\partial\mathbf{N}^T}{\partial y}\frac{\partial\mathbf{N}}{\partial y}\right)dA$$

$$\mathbf{M}=\rho\int_A\left(\mathbf{N}^T\mathbf{N}\right)dA$$

where A and **N** denote the area and shape function of the element, respectively. We herein adopt 4-node plane strain element and **N** is expressed by [N_1, N_2, N_3, N_4].

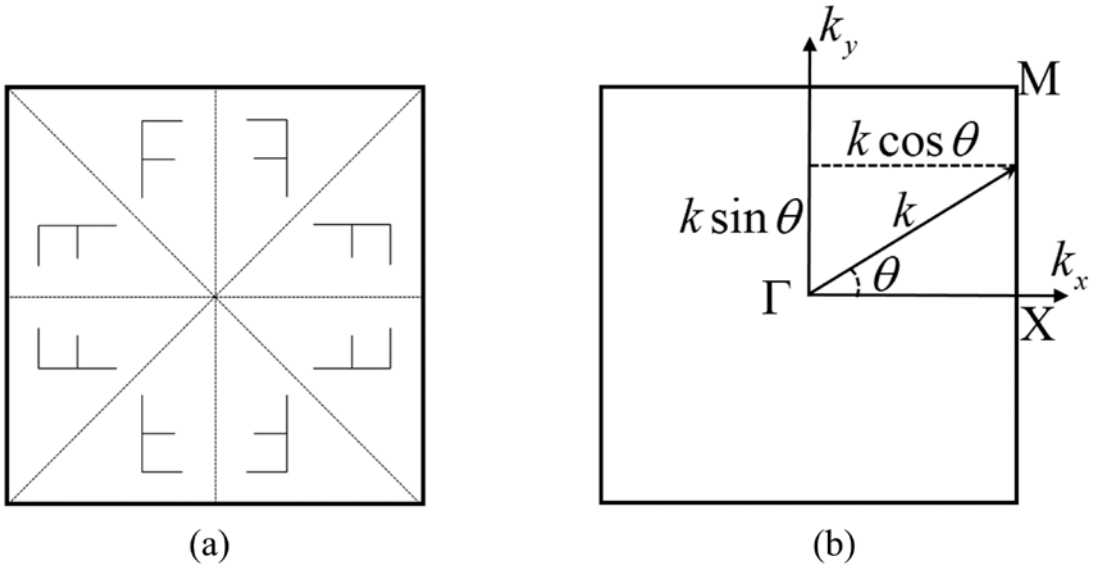

Fig. 1. (a) Unit cell constrained with C_{4v} symmetry. (b) Definitions of the first irreducible Brillouin zone (Γ-X-M-Γ) and the wave vector direction, θ.

As Eq. (3) is a second-order eigenvalue problem in terms of k, which is intractable to be solved. To overcome this difficulty, we convert Eq. (3) into the first-order eigenvalue equation as

$$\left(\mathbf{K}\left(\theta,\omega\right)-k\mathbf{M}\left(\theta\right)\right)\overline{\mathbf{U}}=\mathbf{0} \tag{5}$$

where,

$$\mathbf{K}=\begin{bmatrix}\mathbf{K}_{\mathrm{II}} & \mathbf{K}_{\mathrm{III}}\\ \mathrm{I} & \mathbf{0}\end{bmatrix},\ \mathbf{M}=\begin{bmatrix}-\mathbf{K}_{\mathrm{I}} & \mathbf{0}\\ \mathbf{0} & \mathrm{I}\end{bmatrix},\ \overline{\mathbf{U}}=\begin{bmatrix}k\mathbf{u}\\ \mathbf{u}\end{bmatrix}$$

At the specified ω and θ, Eq. (5) can be solved and the obtained k can be formulated in the form of complex value, $k=k'\pm ik''$, where $k''\geq 0$. Note that $k'+ik''$ and $k'-ik''$ appear in pairs and we only consider $k=k'+ik''$ herein. Previous studies indicate that, within the bandgap, the minimum k'' does not equal to zero and the wave decays in an exponential way dominated by this value [45-47]. Thus, if we maximize the minimum k'', the directional bandgap at the wave vector direction, θ, will be opened at the given frequency, ω.

2.2 Topology optimization formulation

2.2.1 Optimization problem statement

As odd-order bandgap is the prerequisite for designing the SPTI [14, 36-42], topology optimization herein aims to design PCs with two odd-order bandgaps opened around customized frequencies, ω_1 and ω_2, for supporting dual-band corner states. During the optimization, the unit cell is constrained with C_{4v} symmetry, as indicated by Fig. 1(a). An omnidirectional bandgap could be opened by simultaneously maximizing the minimum k'' at all wave vector directions within the first irreducible Brillioun zone, i.e., $\theta \in \left[0, \frac{\pi}{4}\right]$ [see Fig. 1(b)]. To balance the computational efficiency and optimization accuracy, five equally divided wave vector directions between 0° and $\frac{\pi}{4}$ are selected. We discretize the UC with finite elements and assign each element with the design variable, x_e, where $x_e = 0$ denotes material phase 1 and $x_e = 1$ represents material phases 2. Therefore, to create double omnidirectional bandgaps, the optimization formulation should be expressed as

$$\begin{cases} \max: \ f(x_e) = \min\left(k''_{\theta_g,\omega_w}\right) \\ \text{s.t.}: \ \theta_g \in \left[0 : \frac{\pi}{16} : \frac{\pi}{4}\right] \\ \qquad \omega_w \in (\omega_1, \omega_2) \\ \qquad x_e = 0 \text{ or } 1;\ e = 1, 2, \cdots, m \end{cases} \tag{6}$$

in which *m* denotes the number of elements. k''_{θ_g,ω_w} denotes the minimum imaginary part of the wave vector at direction θ_g of frequency ω_w. Totally, ten k''_{θ_g,ω_w} are considered. However, only the minimum one is selected as the objective function and its location often changes between different k''_{θ_g,ω_w} during the iteration, which could cause the numerical instability. To overcome this difficulty, we modify the objective function by considering all k''_{θ_g,ω_w}. At first, we introduce a bound C_1 near the $\min\left(k''_{\theta_g,\omega_w}\right)$, given as

$$C_1 = \begin{cases} 1.1\min\left(k''_{\theta_g,\omega_w}\right) & \text{when } k''_{\theta_g,\omega_w} > 0 \\ 0.1 & \text{when } k''_{\theta_g,\omega_w} < 0 \end{cases} \tag{7}$$

Then, the objective function is adjusted by

$$\overline{f}\left(x_e\right) = \sum_{w=1}^{2}\sum_{g=1}^{5} w_{2(w-1)+g} k''_{\theta_g,\omega_w} \tag{8}$$

where $w_{2(w-1)+g}$ is the weight factor, defined by

$$w_{2(w-1)+g} = \frac{Q_{2(w-1)+g}}{\sum_{w=1}^{2}\sum_{g=1}^{5} Q_{2(w-1)+g}} \tag{9}$$

where $Q_{2(w-1)+g}$ is defined by

$$Q_{2(w-1)+g} = \begin{cases} C_1 - k''_{\theta_g,\omega_w} & \text{when } k''_{\theta_g,\omega_w} < C_1 \\ 0 & \text{when } k''_{\theta_g,\omega_w} > C_1 \end{cases} \tag{10}$$

As a result, $\sum_{w=1}^{2}\sum_{g=1}^{5} w_{2(w-1)+g} = 1$.

2.2.1 Sensitivity analysis

As we adopt gradient-based topology optimization method to update the design variables, the sensitivity, i.e. the derivative of the modified objective function, $\overline{f}\left(x_e\right)$, about the design variable, x_e, should be calculated. According to Eq. (8), the sensitivity of each element can be expressed by

$$\alpha_e = \frac{\partial \overline{f}\left(x_e\right)}{\partial x_e} = \sum_{w=1}^{2}\sum_{g=1}^{5} w_{2(w-1)+g} \frac{\partial k''_{\theta_g,\omega_w}}{\partial x_e} \tag{11}$$

To derive $\frac{\partial k''_{\theta_g,\omega_w}}{\partial x_e}$, we differentiate Eq. (3) with regard to the design variable, x_e, and get

$$\frac{\partial\left(\left(k^2\mathbf{K}_{\mathrm{I}}+k\mathbf{K}_{\mathrm{II}}+\mathbf{K}_{\mathrm{III}}\right)\mathbf{u}\right)}{\partial x_e}=\frac{\partial k}{\partial x_e}\left(2k\mathbf{K}_{\mathrm{I}}\mathbf{u}+\mathbf{K}_{\mathrm{II}}\mathbf{u}\right)+\left(k^2\frac{\partial\mathbf{K}_{\mathrm{I}}}{\partial x_e}+k\frac{\partial\mathbf{K}_{\mathrm{II}}}{\partial x_e}+\frac{\partial\mathbf{K}_{\mathrm{III}}}{\partial x_e}\right)\mathbf{u}$$
$$+\left(k^2\mathbf{K}_{\mathrm{I}}+k\mathbf{K}_{\mathrm{II}}+\mathbf{K}_{\mathrm{III}}\right)\frac{\partial\mathbf{u}}{\partial x_e}=0 \tag{12}$$

To remove $\frac{\partial\mathbf{u}}{\partial x_e}$, we premultiply Eq. (12) with a left-eigenvector $\mathbf{v}^T$ and get

$$\frac{\partial k}{\partial x_e}\left(2k\mathbf{v}^T\mathbf{K}_{\mathrm{I}}\mathbf{u}+\mathbf{v}^T\mathbf{K}_{\mathrm{II}}\mathbf{u}\right)+\mathbf{v}^T\left(k^2\frac{\partial\mathbf{K}_{\mathrm{I}}}{\partial x_e}+k\frac{\partial\mathbf{K}_{\mathrm{II}}}{\partial x_e}+\frac{\partial\mathbf{K}_{\mathrm{III}}}{\partial x_e}\right)\mathbf{u}+\mathbf{v}^T\left(k^2\mathbf{K}_{\mathrm{I}}+k\mathbf{K}_{\mathrm{II}}+\mathbf{K}_{\mathrm{III}}\right)\frac{\partial\mathbf{u}}{\partial x_{ie}}=0 \tag{13}$$

where $\frac{\partial\mathbf{u}}{\partial x_{ie}}$ can be eliminated by selecting

$$\mathbf{v}^T\left(k^2\mathbf{K}_{\mathrm{I}}+k\mathbf{K}_{\mathrm{II}}+\mathbf{K}_{\mathrm{III}}\right)=0 \tag{14}$$

In doing so, $\frac{\partial k}{\partial x_e}$ can be derived as

$$\frac{\partial k}{\partial x_e}=-\frac{\mathbf{v}^T\left(k^2\frac{\partial\mathbf{K}_{\mathrm{I}}}{\partial x_e}+k\frac{\partial\mathbf{K}_{\mathrm{II}}}{\partial x_e}+\frac{\partial\mathbf{K}_{\mathrm{III}}}{\partial x_e}\right)\mathbf{u}}{2k\mathbf{v}^T\mathbf{K}_{\mathrm{I}}\mathbf{u}+\mathbf{v}^T\mathbf{K}_{\mathrm{II}}\mathbf{u}} \tag{15}$$

Then, $\frac{\partial k''_{\theta_g,\omega_w}}{\partial x_e}$ can be calculated as

$$\frac{\partial k''_{\theta_g,\omega_w}}{\partial x_e}=\mathrm{imag}\left(\frac{\partial k_{\theta_g,\omega_w}}{\partial x_e}\right) \tag{16}$$

Based on the calculated sensitivity of each element, the design variable of the element with higher sensitivity will be increased whereas that with lower sensitivity will be decreased. The detailed update scheme will be discussed in the next section.

2.2.3 Updating design variables

Upon obtaining the element sensitivities, the Bi-directional evolutionary structure optimization algorithm (BESO) [48, 49] is utilized to update the design variables iteratively. To make the

optimization process stable, we further the average element sensitivities with their values in the last iteration, that is

$$\alpha_e^r = \frac{1}{2}\left(\alpha_e^{r-1} + \alpha_e^r\right) \tag{17}$$

in which *r* denotes the iteration number.

BESO begins with an initial configuration almost filled with material phase 1. The volume fraction of material phase 1 is V_1. Then V_1 gradually decrease to a settled value V_1^* following

$$V_1^{r+1} = \max\left[V_1^r\left(1-ER\right), V_1^*\right] \tag{18}$$

where *ER* denotes the evolution rate, which is set to be 2% herein.

Based on the calculated sensitivity, the threshold of the sensitivity, α_{th}^r, can be obtained by using the bi-section method to guarantee that, in the next iteration, the volume fraction of material phase 1 equals to V_1^{r+1}. Then, the design variable can be updated following

$$x_e^{r+1} = \begin{cases} \min(x_e^r + \Delta x,\ 1), & \text{if } \alpha_e^r > \alpha_{th}^r \\ \max(x_e^r - \Delta x,\ 0), & \text{if } \alpha_e^r < \alpha_{th}^r \end{cases} \tag{19}$$

where Δx is set as 0.1 herein. The detained optimization process includes the following steps:

Step 1: Set the initial structure and BESO parameters.

Step 2: Calculate complex wave vector **k** and eigenvectors **u** based on Eq. (5).

Step 3: Calculate the objective function $\overline{f}\left(x_e\right)$ based on Eq. (8) and derive the element sensitivity according to Eqs. (14-16).

Step 4: Average the sensitivity with its last iteration value based on Eq. (17) and determine the volume fraction in the next iteration based on Eq. (18).

Step 5: Update design variables based on Eq. (19).

Step 6: Rerun Steps 2-5 until the objective function is maximized.

3. Results and discussions

3.1 Optimized trivial and nontrivial UCs

The material phases 1 and 2 of the PC are assumed to be Aluminum (Al) and Tungsten (W), which are denoted in UCs with black and yellow colors, respectively. Their material parameters are ρ_1=2692 kg/m^3, μ_1=27.9 GPa for Al, and ρ_2=19300 kg/m^3, μ_2=151.4 GPa for W. For brevity, the frequency is standardized as $\Omega = \omega a / 2\pi C_t$, in which $C_t = \sqrt{\mu_1 / \rho_1}$ denotes the speed of transverse waves in Al. In the algorithm, $\Omega_1 = \omega_1 a / 2\pi C_t$ and $\Omega_2 = \omega_2 a / 2\pi C_t$ are customized parameters for controlling the positions of the first and the second objective bandgaps, which could produce the on-demand solution according to the practical applications. As noted before, only dual odd-order bandgaps satisfy the condition for hosting dual-band corner states, we conduct many numerical experiments and select four representative results with dual odd-order bandgaps to present herein. These results are obtained by setting (Ω_1, Ω_2) to be (0.8, 1.1), (1.0, 2.5), (1.0, 2.7) and (1.0, 3.0), signified by Case 1, Case 2, Case 3, Case 4, respectively, which will be analyzed detailedly in the following. Figure 2 presents the evolution process of the UC in Case 3, one can see that the UC begins with a nearly uniform structure with the objective value of zero and gradually evolves into the optimal configuration with the maximized objective value. The vibration of the objective value during the optimization process is mainly due to the jump of the minimum k'' between different wave vectors, demonstrating the complexity of the optimization problem. Nevertheless, the solution could be successfully obtained.

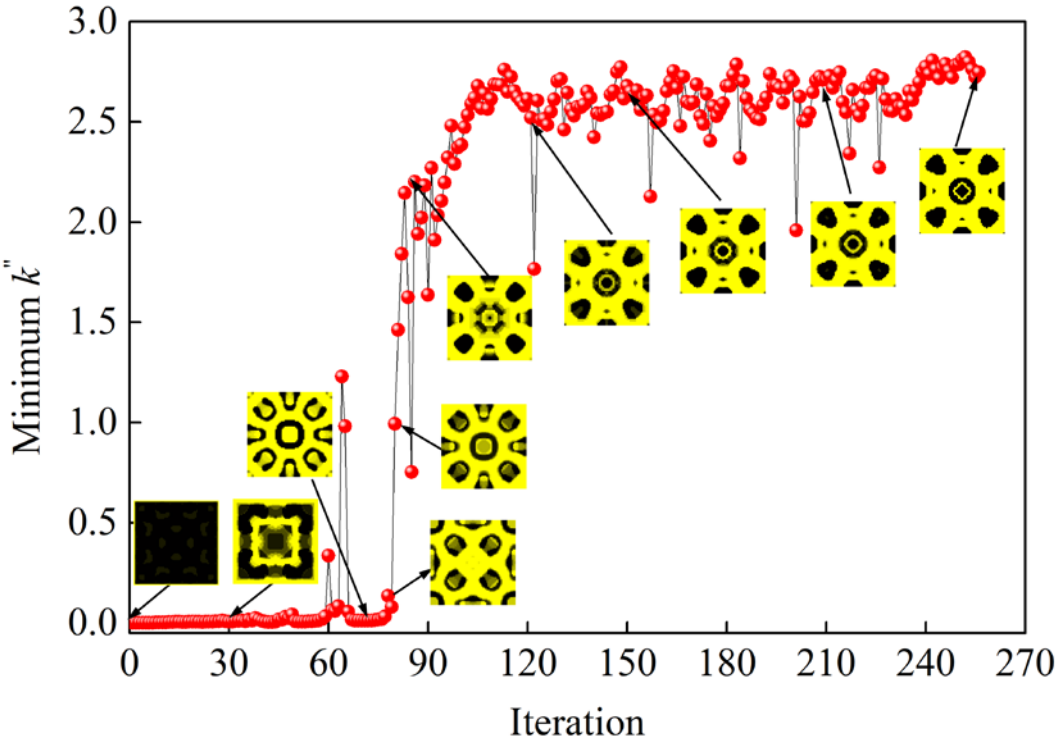

Fig. 2. Evolution process of the UC3 and the objective value.

Figures 3-6(a) show the optimized PCs for Cases 1-4, where the primitive UCs are denoted within the blue dashed box and labeled by UC*i*A (*i* denotes the number of the Case), respectively. These configurations have never been reported before. The band structures of the optimized PCs are presented in Figs. 3-6(b). It can be seen that two objective bandgaps are successfully formed around the setting values of Ω_1 and Ω_2, which are marked by blue and red areas, respectively. Table 1 summarizes the frequency range, midgap-gap-ratio (GR) and order (that is, number of bands below the band gap) of these two band gaps. It can be see that the band orders and frequency ranges of the dual band gaps for these optimization results are different, resulting in different frequencies of the dual-band corner states, which will be discussed in the following.

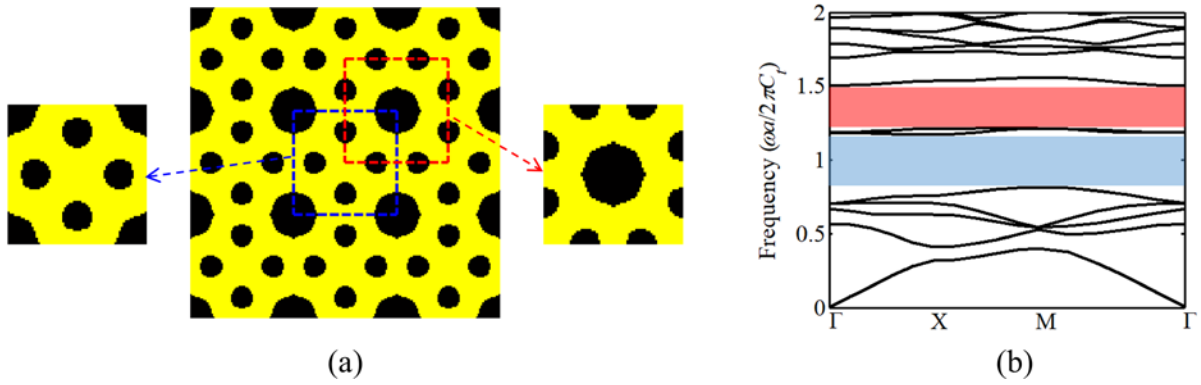

Fig. 3. The Optimized PC and its band structure for Case 1. (a) The optimized PC consisting of 3×3 UCs. (b) The band structure.

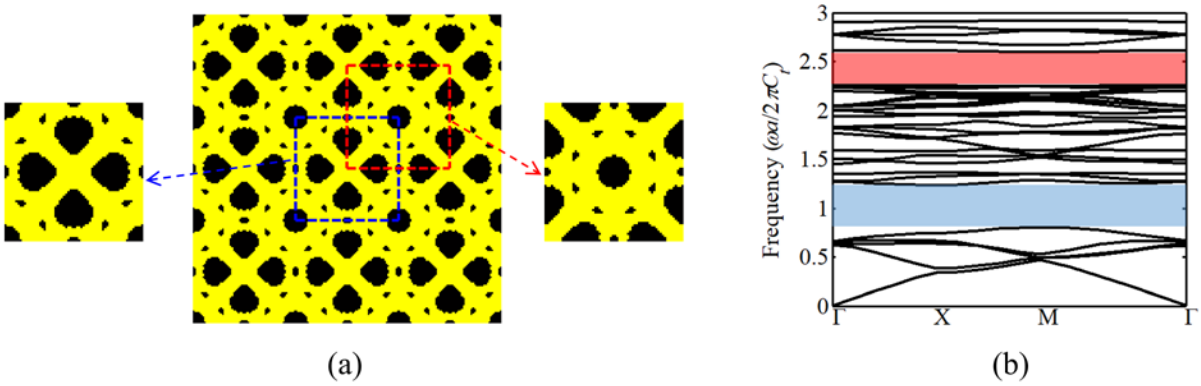

Fig. 4. The Optimized PC and its band structure for Case 2. (a) The optimized PC consisting of 3×3 UCs. (b) The band structure.

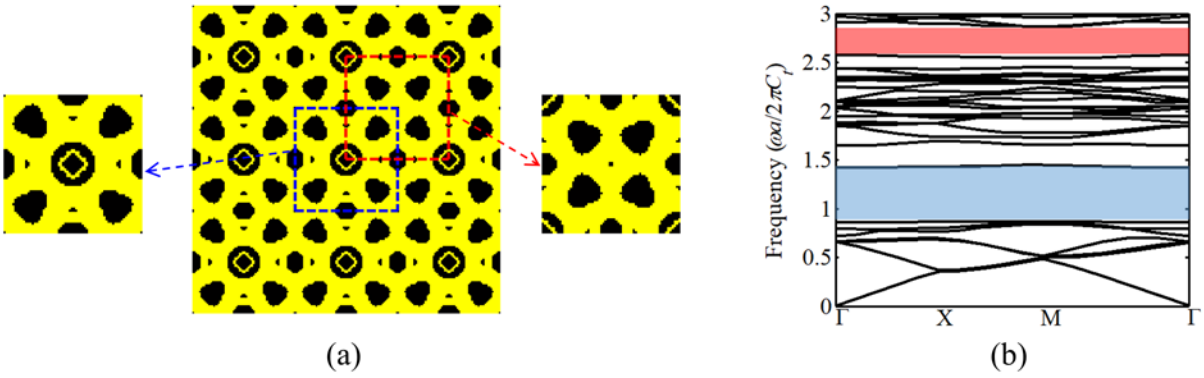

Fig. 5. The Optimized PC and its band structure for Case 3. (a) The optimized PC consisting of 3×3 UCs. (b) The band structure.

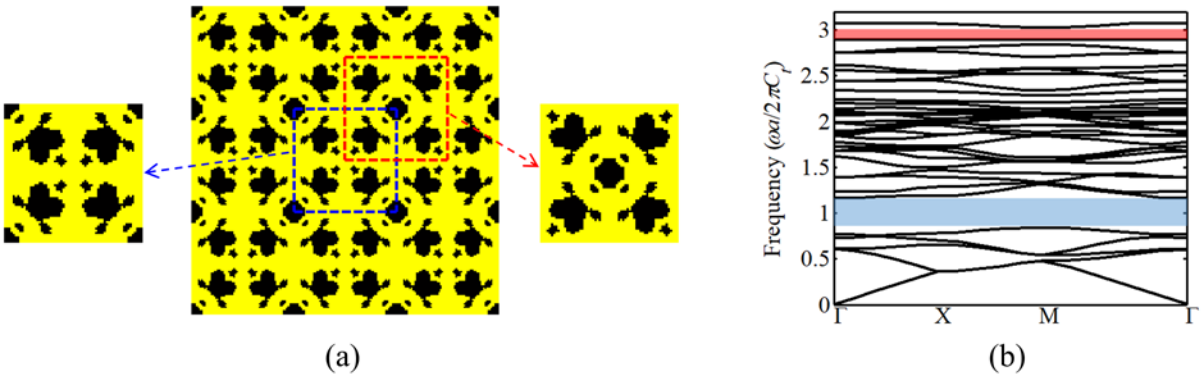

Fig. 6. The Optimized PC and its band structure for Case 4. (a) The optimized PC consisting of 3×3 UCs. (b) The band structure.

Table 1. The frequency ranges and orders of two objective band gaps.

	The first objective band gap			The second objective band gap		
	Frequency range	GR(%)	Order	Frequency range	GR(%)	Order
Case 1	0.812-1.169	36.0	5	1.210-1.566	25.7	7
Case 2	0.805-1.231	41.9	5	2.255-2.596	14.1	25
Case 3	0.865-1.417	48.4	7	2.577-2.868	10.7	27
Case 4	0.844-1.161	31.6	5	2.892-3.025	4.5	35

Generally, constructing the SPTI needs to create two kinds of UCs with distinct topological properties. As indicated by previous studies on second-order photonic topological insulators, selecting UCs from the same PC supporting odd-order bandgaps in distinct ways could lead to different topological properties [14, 42]. Table 1 shows that all bandgaps are odd-order, thus we can use these optimized to further construct SPTIs. To create the UC with a different topological property from the primitive UC, we translate the primitive UC along $\left(\frac{a}{2},\frac{a}{2}\right)$ and get the new UC labeled by UC*i*B, which is represented by the red dashed box. As UC*i*A and UC*i*B encode the same PC, they have the same band structures. Nonetheless, the topological properties of the bandgap for UC*i*A and UC*i*B could be different.

Next, we use the 2D polarization $\mathbf{P}=\left(P_x,P_y\right)$ to characterize the topological properties of UC*i*As and UC*i*Bs, which can be calculated by [50-53]

$$P_l=\frac{1}{2}\left(\sum_n q_l^n \text{modulo } 2\right), \qquad (-1)^{q_l^n}=\frac{\eta_n\left(\mathrm{X}_l\right)}{\eta_n\left(\Gamma\right)} \tag{20}$$

where $l=x,y$ is the direction and $P_x=P_y$ because the optimized PCs own the C_{4v} symmetry. η_n is the parity of the *n*-th band at the high symmetry points Γ and X_l, which can be calculated according to the eigenmode profile, i.e., the parity of *p* mode is odd, while the parity of *s* and *d* modes is even (+). $\sum_n q_l^n$ denotes the summation of q_l^n for all bands below the objective bandgap. From Eq. (20), we can also derive a simple rule to calculate the **P** via the number of pairs of parities with opposite signs at Γ and X for the same band below the objective bandgap, that is, while an odd number of pairs get $\mathbf{P}=\left(\frac{1}{2},\frac{1}{2}\right)$, an even number implies $\mathbf{P}=\left(0,0\right)$. Table 2 gives the parities at Γ and X_i of all bands below the second objective bandgap for all UC*i*As and UC*i*Bs, where parities with opposite signs at Γ and X for the same band are shaded with blue colors. Accordingly, we can get that, for the first objective bandgap, $\mathbf{P}=\left(\frac{1}{2},\frac{1}{2}\right)$ for UC1A, UC2A, UC3A and UC4A, while $\mathbf{P}=\left(0,0\right)$ for UC1B, UC2B, UC3B and UC4B; for the second objective bandgap, $\mathbf{P}=\left(\frac{1}{2},\frac{1}{2}\right)$ for UC1A, UC2B, UC3A and UC4A, while $\mathbf{P}=\left(0,0\right)$ for UC1B, UC2A, UC3B and UC4B. Note that $\mathbf{P}=\left(\frac{1}{2},\frac{1}{2}\right)$ indicates a nontrivial bandgap while $\mathbf{P}=\left(0,0\right)$ implies a trivial bandgap. Therefore, for the same Case *i*, UC*i*A and UC*i*B have different topological properties for both the first and second objective bandgaps, which will lead to the emergence of topological edge states at the edge between

them. Moreover, the simultaneous nonzero P_x and P_y could lead to a nonzero topological corner charge [50]:

$$Q^c = 4P_xP_y \tag{21}$$

Accordingly, the topological corner charges equal to 1 and 0 for nontrivial and trivial bandgaps, respectively, which enables the presence of topological corner states within both the first and the second bandgaps at a 90° corner between the trivial and nontrivial regions.

Table 2. Parities at Γ and X points of bands below the objective bandgaps for UC*i*As and UC*i*Bs

Band	UC1A		UC1B		UC2A		UC2B		UC3A		UC3B		UC4A		UC4B	
order	Γ	X	Γ	X	Γ	X	Γ	X	Γ	X	Γ	X	Γ	X	Γ	X
1	+	-	+	+	+	+	+	-	+	+	+	-	+	-	+	+
2	+	+	+	-	+	-	+	+	+	-	+	+	-	+	-	-
3	+	-	+	+	+	-	+	+	-	+	-	-	-	-	-	+
4	-	-	-	+	-	-	-	+	-	+	-	-	+	+	+	-
5	-	+	-	-	-	+	-	-	+	-	+	+	+	-	+	+
6	-	+	-	-	-	+	-	-	+	-	+	+	+	+	+	-
7	-	+	-	-	-	+	-	-	+	+	+	-	+	-	+	+
8					+	-	+	+	-	-	-	+	-	+	-	-
9					+	-	+	+	-	-	-	+	-	+	-	-
10					+	-	+	+	+	-	+	+	+	-	+	+
11					+	+	+	-	-	+	-	-	-	-	-	+
12					+	-	+	+	-	+	-	-	-	-	-	+
13					-	+	-	-	+	-	+	+	+	+	+	-
14					-	+	-	-	+	+	+	-	+	+	+	-
15					+	-	+	+	+	-	+	+	-	-	-	+
16					+	+	+	-	-	-	-	+	-	+	-	-
17					-	+	-	-	-	+	-	-	+	+	+	-
18					-	-	-	+	+	+	+	-	+	-	+	+
19					+	-	+	+	-	-	-	+	-	-	-	+
20					-	-	+	+	-	-	-	+	-	+	-	-
21					-	+	+	-	+	+	+	-	+	-	+	+
22					+	-	+	+	+	+	+	-	-	+	-	-
23					+	+	-	-	+	+	+	-	-	+	-	-
24					-	+	-	-	+	-	+	+	+	-	+	+
25					-	+	+	-	-	-	-	+	+	+	+	-
26									-	+	-	-	+	-	+	+
27									+	+	+	-	+	-	+	+
28													-	+	-	-
29													-	-	-	+
30													+	-	+	+
31													+	+	+	-

32	-	+	-	-
33	-	-	-	+
34	-	+	-	-
35	-	+	-	-

3.2 Topological edge states

To validate the topological edge states, for each case, we build a supercell made of six UC*i*As and six UC*i*Bs with an interface between them, as shown in Fig. 7(a). We present the projected band diagrams around the second and first objective bandgaps for Case 1-4 in Figs 8-11 (a) and (b), respectively. One can see that topological edge states emerge within both the first and second objective bandgaps for all cases. Figures 8-11 (c) and (d) plot the eigenmodes of the edge states within the second and first objective bandgaps, respectively, from which we can find that the edge states are indeed localized at the interfaces between UC*i*As and UC*i*Bs, which are topologically protected and thus robust against to defects. Moreover, these gapped edge states satisfy the prerequisite for producing corner states [6, 54].

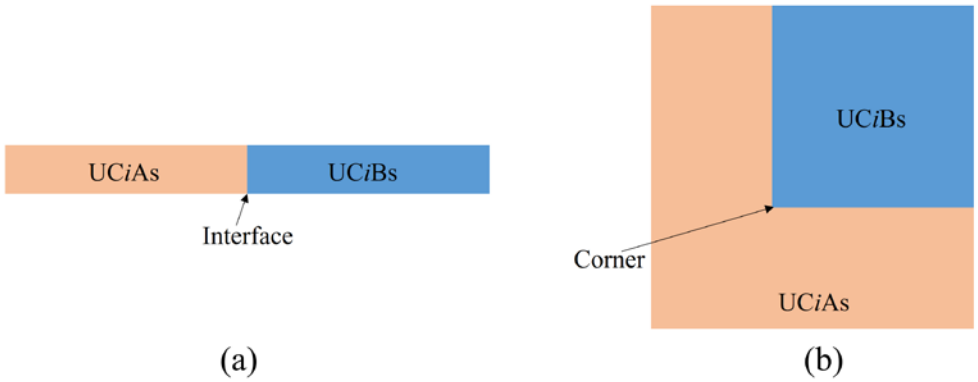

Fig. 7. (a) Schematic of the supercell for calculating edge states. (b) Schematic of the metastructure for calculating corner states.

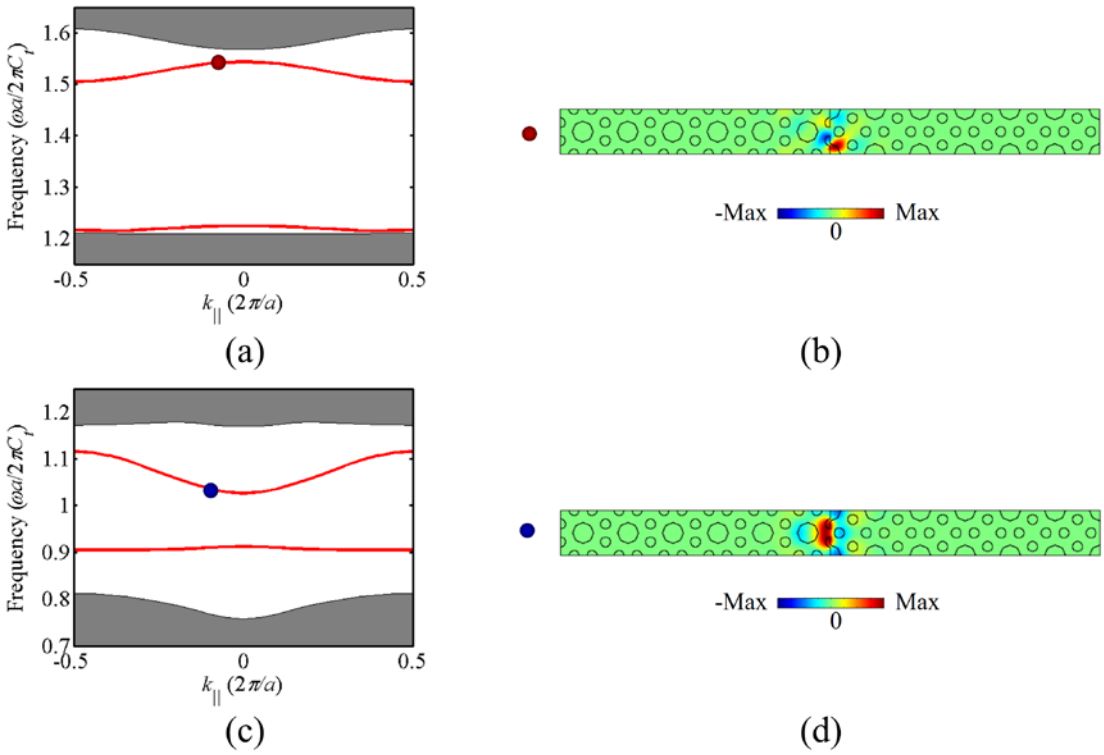

Fig. 8. Projected band diagrams and eigenfields of edge states of the supercell for Case 1. (a), (c) Projected band structures around the second and first objective bandgaps, respectively. (b), (d) Eigenfields of edge states within the second and first objective bandgaps, corresponding to the red and blue balls in (a) and (c), respectively.

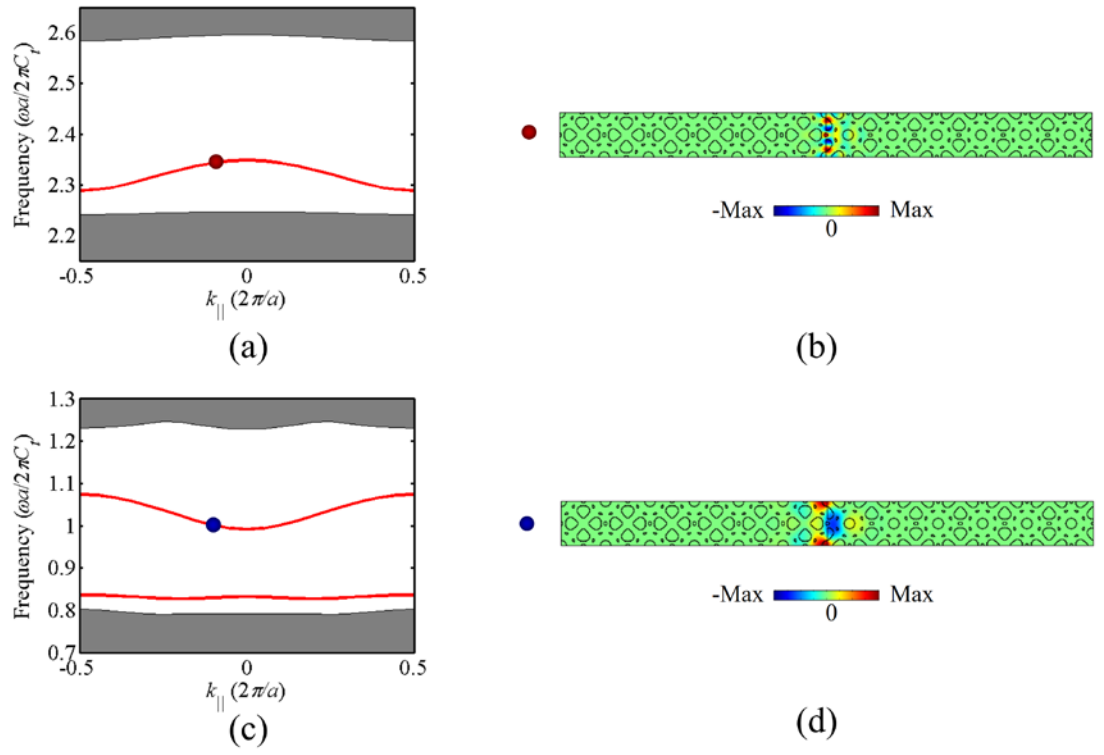

Fig. 9. Projected band diagrams and eigenfields of edge states of the supercell for Case 2. (a), (c) Projected band structures around the second and first objective bandgaps, respectively. (b), (d) eigenfields of edge states within the second and first objective bandgaps, corresponding to the red and blue balls, respectively.

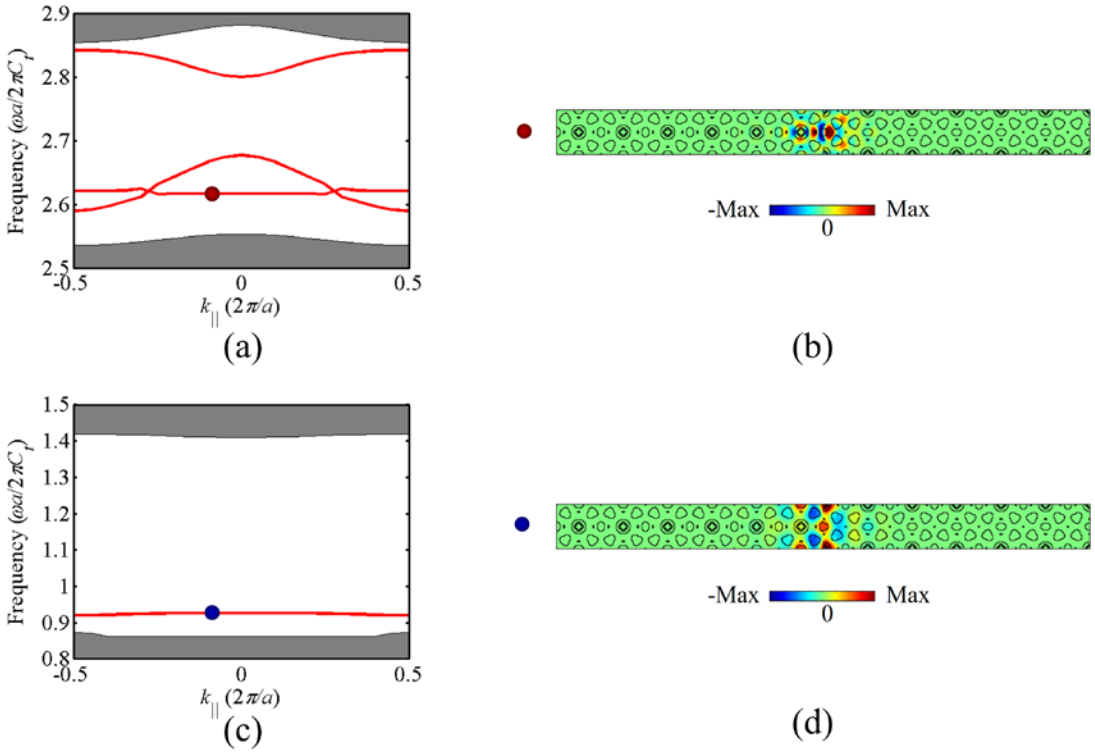

Fig. 10. Projected band diagrams and eigenfields of edge states of the supercell for Case 3. (a), (c) Projected band structures around the second and first objective bandgaps, respectively. (b), (d) eigenfields of edge states within the second and first objective bandgaps, corresponding to the red and blue balls, respectively.

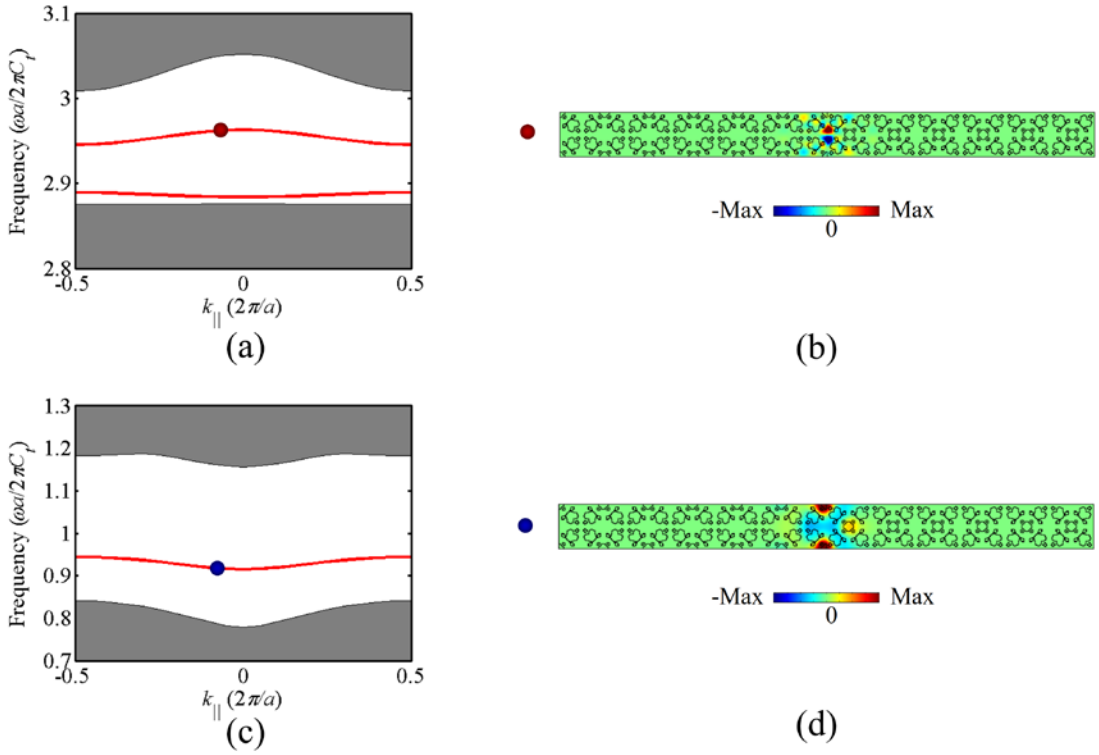

Fig. 11. Projected band diagrams and eigenfields of edge states of the supercell for Case 4. (a), (c) Projected band structures around the second and first objective bandgaps, respectively. (b), (d) eigenfields of edge states within the second and first objective bandgaps, corresponding to the red and blue balls, respectively.

3.3 Topological corner states

To confirm the corner states, we construct the metastructure, as sketched in Fig. 7(b), consisting of 5×5 UC*i*As surrounded by three layers of UC*i*Bs, which is labeled by MS*i* for Case *i*. A corner is formed between the domains of UC*i*As and UC*i*Bs. Figures 12-15 demonstrate the calculated eigenfrequency spectrums for MS1-MS4, respectively, where Figs. 12-15(a) are around the first objective bandgaps, whereas Figs. 12-15(b) are around the second objective bandgaps. We can observe that corners states emerge within both the first and second objective bandgaps. Interestingly, multiple corner states are observed within the first and second objective bandgaps for MS1, the first objective bandgap for MS2 and the second objective bandgap for MS3 and MS4. The reason is that these SPTIs are made of optimized unit cells

with complex configuration, which may lead to strong long-range couplings, thus resulting in multiple corner states emerging inside or outside the gapped edge states. Figures 16-19 plot the eigenfields of corner states labeled in Figs. 12-15, respectively. We can observe that these corner states are tightly localized at the corners which have different profiles and thus provide flexibility in practical applications.

Next, using the MS2 as an example, we verify the robustness of the corner states by introducing the defect. The defect is introduced by removing some material phases 2 within several UCs denoted by red dashed boxes, as sketched in Fig. 20(a). Figure 20(b) shows the calculated eigenfields of corner states for the MS2 with the defect, we can see that these corner states are not destroyed and their eigenfrequencies are not changed compared with those of corner states without the defect shown in Fig. 17, verifying the robustness of these corner states against the defect.

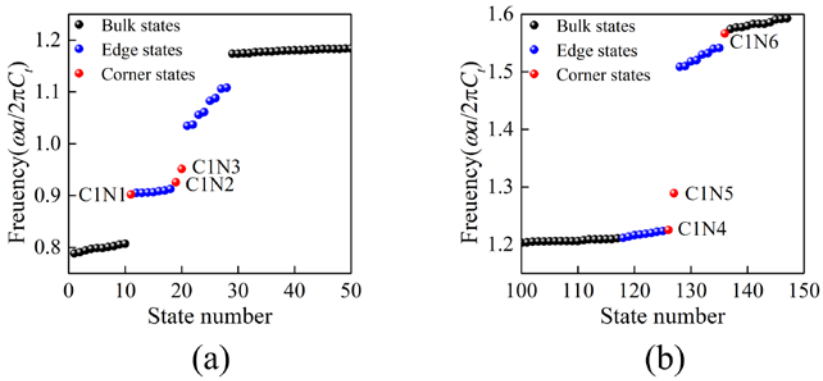

Fig. 12. Eigenfrequency spectrums around the (a) first and (b) second objective bandgaps for MS1.

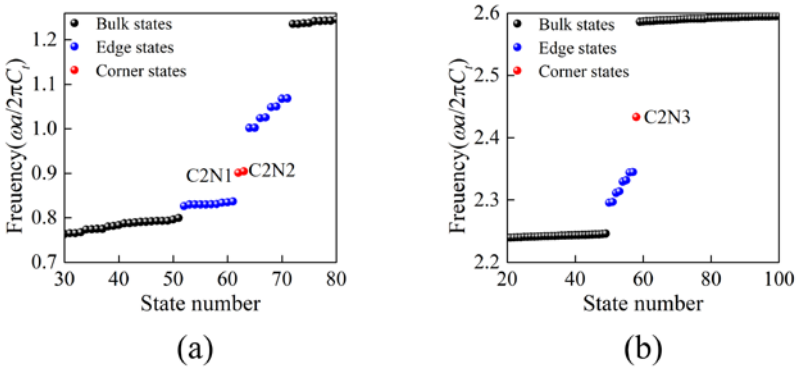

Fig. 13. Eigenfrequency spectrums around the (a) first and (b) second objective bandgaps for MS2.

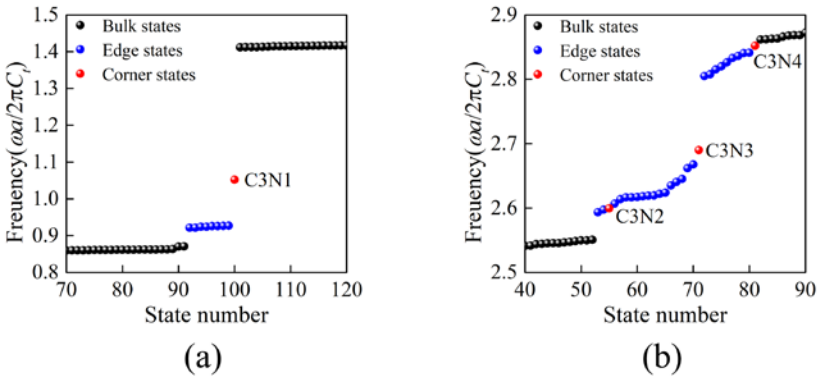

Fig. 14. Eigenfrequency spectrums around the (a) first and (b) second objective bandgaps for MS3.

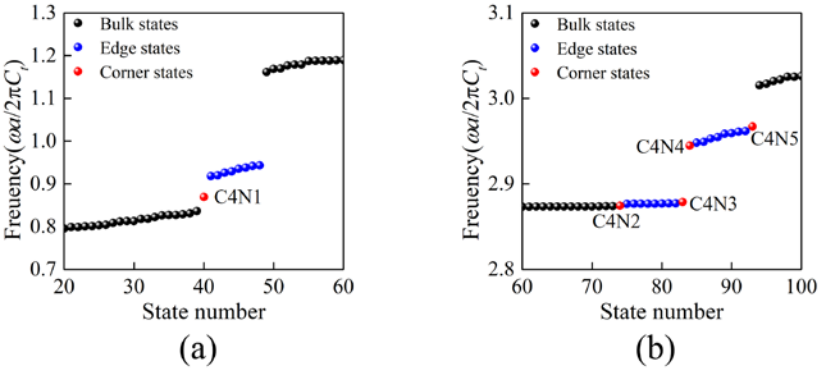

Fig. 15. Eigenfrequency spectrums around the (a) first and (b) second objective bandgaps for MS4.

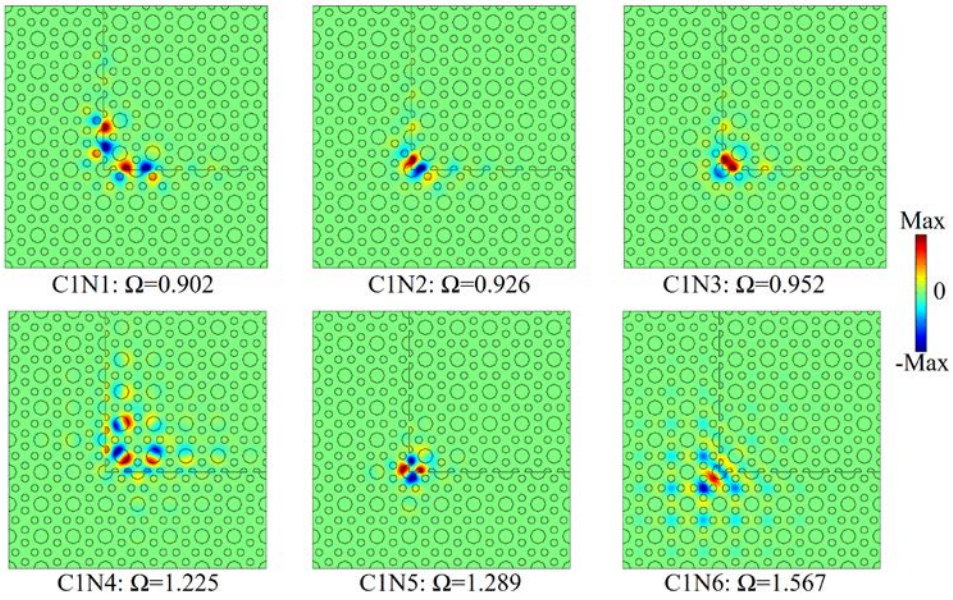

Fig. 16. Eigenfields of corner states labeled in Fig. 12 for MS1.

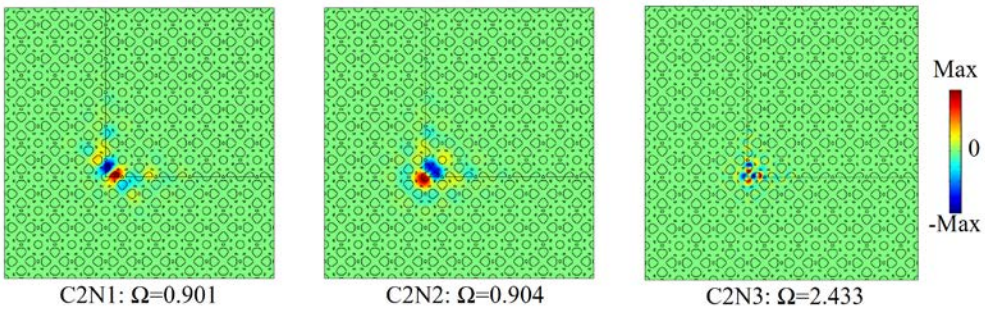

Fig. 17. Eigenfields of corner states labeled in Fig. 13 for MS2.

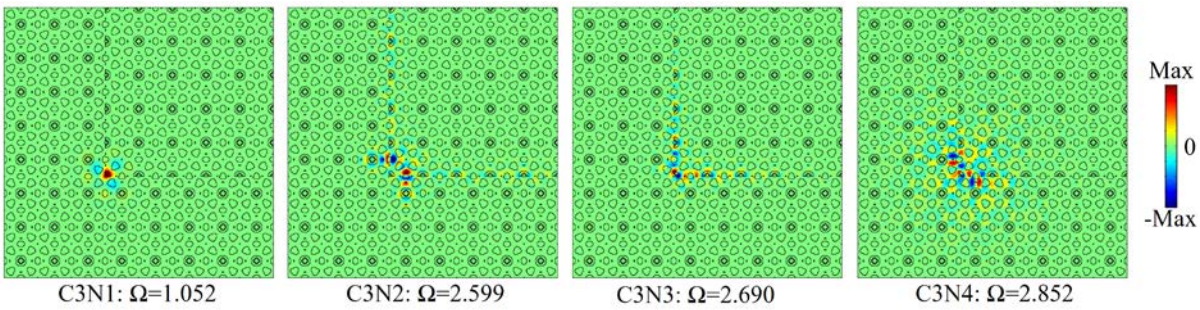

Fig. 18. Eigenfields of corner states labeled in Fig. 14 for MS3.

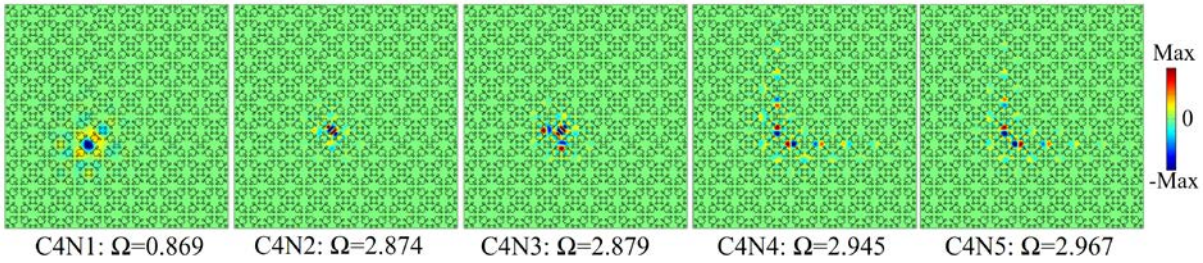

Fig. 19. Eigenfields of corner states labeled in Fig. 15 for MS4.

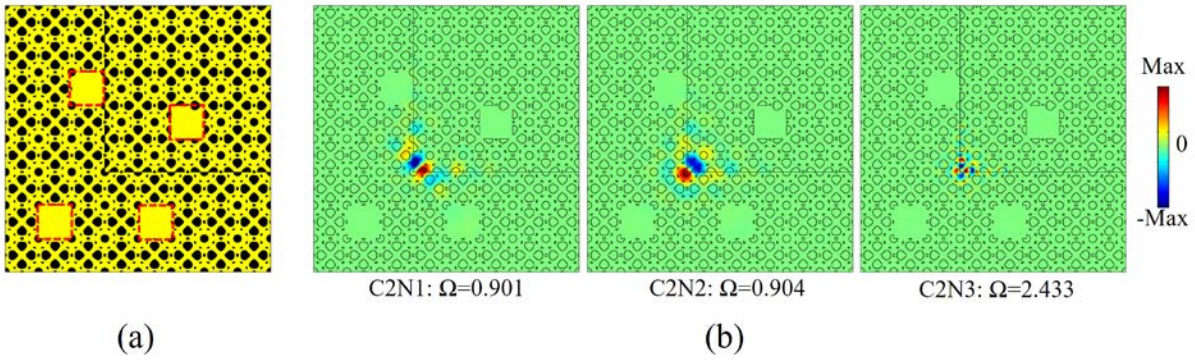

Fig. 20. (a) Schematic of the metastructure with the defect. (b) Eigenfields of corner states of the metastructure in (a).

4. Conclusion

In conclusion, we design four SPTIs with customized dual-bandgaps supporting dual-band corner states by topology optimization. The dual-bandgap is obtained by maximizing minimum imaginary parts of wave vectors at two given frequencies simultaneously. Topological trivial and nontrivial UCs are created by selecting UCs from the optimized PCs in distinct ways. Four SPTIs, built by arranging the trivial and nontrivial UCs, are created, which support tightly localized dual-band corner states. Moreover, some of the optimized structures (e.g. MS1) support multiple corner states in one gap, a property that traditional second-order phononic TIs do not possess, which may provide flexibilities in practical applications. The robustness of dual-band corner states against defects is further verified. The designed SPTIs can find important applications in multiband waveguides, filters and communications with robustness. By engineering the coupling between corner and edge states, the designed SPTIs can be also utilized for realizing dual-band robust Fano resonance, which has important applications in high-sensitivity detections [55]. The design method could be applied to design dual-band corner states in sonic and photonic systems as well.

Acknowledgements

This work is supported by National Natural Science Foundation of China (No. 1210020421), Natural Science Foundation of Hunan Province (2022JJ40026), the Fundamental Research Funds for the Central Universities (Grant No. 22120220237), the Hong Kong Scholars Program (No. XJ2020004) and the Research Grants Council of Hong Kong SAR (Grant No. C6013-18G, AoE/P-502/20, 15205219, 15202820 and 15204419).

References

[1] V. Laude, Phononic Crystals: Artificial Crystals for Sonic, Acoustic, and Elastic Waves, Walter de Gruyter GmbH & Co KG2015.
[2] H. Huang, J. Chen, S. Huo, Recent advances in topological elastic metamaterials, Journal of Physics: Condensed Matter (2021).
[3] P. Wang, L. Lu, K. Bertoldi, Topological phononic crystals with one-way elastic edge waves, Physical review letters 115(10) (2015) 104302.
[4] S.-Y. Yu, C. He, Z. Wang, F.-K. Liu, X.-C. Sun, Z. Li, H.-Z. Lu, M.-H. Lu, X.-P. Liu, Y.-F. Chen, Elastic pseudospin transport for integratable topological phononic circuits, Nature communications 9(1) (2018) 3072.
[5] M. Yan, J. Lu, F. Li, W. Deng, X. Huang, J. Ma, Z. Liu, On-chip valley topological materials for elastic wave manipulation, Nature Materials 17(11) (2018) 993.
[6] B. Xie, H.-X. Wang, X. Zhang, P. Zhan, J.-H. Jiang, M. Lu, Y. Chen, Higher-order band topology, Nature Reviews Physics (2021) 1-13.
[7] H. Fan, H. Gao, S. An, Z. Gu, S. Liang, Y. Zheng, T. Liu, Hermitian and non-hermitian topological edge states in one-dimensional perturbative elastic metamaterials, Mechanical Systems and Signal Processing 169 (2022) 108774.
[8] Y. Wu, M. Yan, Z.-K. Lin, H.-X. Wang, F. Li, J.-H. Jiang, On-chip higher-order topological micromechanical metamaterials, Science Bulletin 66(19) (2021) 1959-1966.
[9] C.-W. Chen, R. Chaunsali, J. Christensen, G. Theocharis, J. Yang, Corner states in a second-order mechanical topological insulator, Communications Materials 2(1) (2021) 62.
[10] H. Fan, B. Xia, L. Tong, S. Zheng, D. Yu, Elastic higher-order topological insulator with topologically protected corner states, Physical review letters 122(20) (2019) 204301.
[11] Q. Wu, H. Chen, X. Li, G. Huang, In-plane second-order topologically protected states in elastic Kagome lattices, Physical Review Applied 14(1) (2020) 014084.
[12] S. An, T. Liu, H. Fan, H. Gao, Z. Gu, S. Liang, S. Huang, Y. Zheng, Y. Chen, L. Cheng, Second-order elastic topological insulator with valley-selective corner states, International Journal of Mechanical Sciences 224 (2022) 107337.
[13] Z.-D. Zhang, S.-Y. Yu, M.-H. Lu, Y.-F. Chen, Electrically tunable topological interface states in one-dimensional nanomechanical lattices, Physical Review B 105(13) (2022) 134102.
[14] Y. Chen, Z. Lan, J. Li, J. Zhu, Topologically protected second harmonic generation via doubly resonant high-order photonic modes, Physical Review B 104(15) (2021) 155421.
[15] M.P. Bendsoe, O. Sigmund, Topology optimization: theory, methods, and applications, Springer Science & Business Media2013.
[16] J.S. Jensen, O. Sigmund, Topology optimization for nano-photonics, Laser & Photonics Reviews 5(2) (2011) 308-321.
[17] W. Li, F. Meng, Y. Chen, Y.f. Li, X. Huang, Topology Optimization of Photonic and

Phononic Crystals and Metamaterials: A Review, Advanced Theory and Simulations 1900017.
[18] S. Molesky, Z. Lin, A.Y. Piggott, W. Jin, J. Vucković, A.W. Rodriguez, Inverse design in nanophotonics, Nature Photonics 12(11) (2018) 659.
[19] G.L. Yi, B.D. Youn, A comprehensive survey on topology optimization of phononic crystals, Structural and Multidisciplinary Optimization 54(5) (2016) 1315-1344.
[20] J. Guo, X. Zhang, Y. Fang, Topology optimization design and experimental validation of an acoustic metasurface for reflected wavefront modulation, Journal of Sound and Vibration 520 (2022) 116631.
[21] A. Takezawa, T. Yamamoto, X. Zhang, K. Yamakawa, S. Nakano, M. Kitamura, An objective function for the topology optimization of sound-absorbing materials, Journal of Sound and Vibration 443 (2019) 804-819.
[22] J. Desai, A. Faure, G. Michailidis, G. Parry, R. Estevez, Topology optimization in acoustics and elasto-acoustics via a level-set method, Journal of Sound and Vibration 420 (2018) 73-103.
[23] X.W. Yang, J.S. Lee, Y.Y. Kim, Effective mass density based topology optimization of locally resonant acoustic metamaterials for bandgap maximization, Journal of Sound and Vibration 383 (2016) 89-107.
[24] X. Zhang, J. He, A. Takezawa, Z. Kang, Robust topology optimization of phononic crystals with random field uncertainty, International Journal for Numerical Methods in Engineering 115(9) (2018) 1154-1173.
[25] R.E. Christiansen, F. Wang, O. Sigmund, Topological insulators by topology optimization, Physical Review Letters 122(23) (2019) 234502.
[26] R.E. Christiansen, F. Wang, O. Sigmund, S. Stobbe, Designing photonic topological insulators with quantum-spin-Hall edge states using topology optimization, Nanophotonics 8(8) (2019) 1363-1369.
[27] J. Luo, Z. Du, C. Liu, Y. Mei, W. Zhang, X. Guo, Moving Morphable Components-based inverse design formulation for quantum valley/spin hall insulators, Extreme Mechanics Letters 45 (2021) 101276.
[28] S. Nanthakumar, X. Zhuang, H.S. Park, C. Nguyen, Y. Chen, T. Rabczuk, Inverse design of quantum spin hall-based phononic topological insulators, Journal of the Mechanics and Physics of Solids 125 (2019) 550-571.
[29] Y. Chen, F. Meng, B. Jia, G. Li, X. Huang, Inverse Design of Photonic Topological Insulators with Extra-Wide Bandgaps, Physica Status Solidi-Rapid Research Letters 13(9) (2019) 1900175
[30] Y. Chen, F. Meng, X. Huang, Creating acoustic topological insulators through topology optimization, Mechanical Systems and Signal Processing 146 (2021) 107054.
[31] Z. Du, H. Chen, G. Huang, Optimal quantum valley Hall insulators by rationally engineering Berry curvature and band structure, Journal of the Mechanics and Physics of Solids 135 (2020) 103784.
[32] J. Zhang, F. Wang, O. Sigmund, L. Gao, R.E. Christiansen, Ultra-broadband edge-state pair for zigzag-interfaced valley Hall insulators, Science China Physics, Mechanics & Astronomy 65(5) (2022) 1-9.
[33] Y. Chen, J. Li, J. Zhu, Topology optimization of quantum spin Hall effect-based second-order phononic topological insulator, Mechanical Systems and Signal Processing 164 (2022) 108243.
[34] Y. Chen, On the use of topology optimized band gap structures for the realization of second-order acoustic topological insulators with valley-selective corner states, Structural and Multidisciplinary Optimization 65(4) (2022) 1-11.
[35] Y. Chen, Z. Lan, J. Zhu, Inversely Designed Second-Order Photonic Topological Insulator With Multiband Corner States, Physical Review Applied 17(5) (2022) 054003.

[36] X.-D. Chen, W.-M. Deng, F.-L. Shi, F.-L. Zhao, M. Chen, J.-W. Dong, Direct observation of corner states in second-order topological photonic crystal slabs, Physical Review Letters 122(23) (2019) 233902.
[37] B.-Y. Xie, H.-F. Wang, H.-X. Wang, X.-Y. Zhu, J.-H. Jiang, M.-H. Lu, Y.-F. Chen, Second-order photonic topological insulator with corner states, Physical Review B 98(20) (2018) 205147.
[38] B.-Y. Xie, G.-X. Su, H.-F. Wang, H. Su, X.-P. Shen, P. Zhan, M.-H. Lu, Z.-L. Wang, Y.-F. Chen, Visualization of higher-order topological insulating phases in two-dimensional dielectric photonic crystals, Physical Review Letters 122(23) (2019) 233903.
[39] L. Zhang, Y. Yang, Z.-K. Lin, P. Qin, Q. Chen, F. Gao, E. Li, J.-H. Jiang, B. Zhang, H. Chen, Higher-Order Topological States in Surface-Wave Photonic Crystals, Advanced Science 7(6) (2020) 1902724.
[40] Y. Ota, F. Liu, R. Katsumi, K. Watanabe, K. Wakabayashi, Y. Arakawa, S. Iwamoto, Photonic crystal nanocavity based on a topological corner state, Optica 6(6) (2019) 786-789.
[41] Z.-G. Chen, C. Xu, R. Al Jahdali, J. Mei, Y. Wu, Corner states in a second-order acoustic topological insulator as bound states in the continuum, Physical Review B 100(7) (2019) 075120.
[42] Y. Chen, Z. Lan, J. Zhu, Second-order topological phases in C 4v -symmetric photonic crystals beyond the two-dimensional Su-Schrieffer–Heeger model, Nanophotonics 11(7) (2022) 1345-1354.
[43] L. Wang, H. Zheng, X. Lu, L. Shi, A Petrov-Galerkin finite element interface method for interface problems with Bloch-periodic boundary conditions and its application in phononic crystals, Journal of Computational Physics 393 (2019) 117-138.
[44] C. Kittel, Introduction to solid state physics : 6th ed, American Journal of Physics 61(1) (2011) 59.
[45] V. Laude, Y. Achaoui, S. Benchabane, A. Khelif, Evanescent Bloch waves and the complex band structure of phononic crystals, Physical Review B 80(9) (2009) 092301.
[46] V. Romero-García, J. Sánchez-Pérez, S. Castiñeira-Ibáñez, L. Garcia-Raffi, Evidences of evanescent Bloch waves in phononic crystals, Applied Physics Letters 96(12) (2010) 124102.
[47] Y.-F. Wang, Y.-S. Wang, V. Laude, Wave propagation in two-dimensional viscoelastic metamaterials, Physical Review B 92(10) (2015) 104110.
[48] X.Y. Yang, Y.M. Xie, G. Steven, O. Querin, Bidirectional evolutionary method for stiffness optimization, AIAA journal 37(11) (1999) 1483-1488.
[49] Y.M. Xie, G.P. Steven, A simple evolutionary procedure for structural optimization, Computers & structures 49(5) (1993) 885-896.
[50] F. Liu, H.-Y. Deng, K. Wakabayashi, Helical Topological Edge States in a Quadrupole Phase, Physical Review Letters 122(8) (2019) 086804.
[51] Z. Zhang, M.R. López, Y. Cheng, X. Liu, J. Christensen, Non-Hermitian sonic second-order topological insulator, Physical review letters 122(19) (2019) 195501.
[52] Z. Zhang, H. Long, C. Liu, C. Shao, Y. Cheng, X. Liu, J. Christensen, Deep-Subwavelength Holey Acoustic Second-Order Topological Insulators, Advanced Materials 31(49) (2019) 1904682.
[53] W.A. Benalcazar, T. Li, T.L. Hughes, Quantization of fractional corner charge in C n-symmetric higher-order topological crystalline insulators, Physical Review B 99(24) (2019) 245151.
[54] X. Zhang, H.-X. Wang, Z.-K. Lin, Y. Tian, B. Xie, M.-H. Lu, Y.-F. Chen, J.-H. Jiang, Second-order topology and multidimensional topological transitions in sonic crystals, Nature Physics 15(6) (2019) 582-588.
[55] O. Kang-Hyok, K.-H. Kim, Ultrahigh-Q Fano resonance using topological corner modes in second-order pseudospin-Hall photonic systems, Optics & Laser Technology 147 (2022)

107616.